HHS Public Access

Author manuscript

Phys Med Biol. Author manuscript; available in PMC 2020 May 02.

Published in final edited form as:

Phys Med Biol. ; 64(9): 095023. doi:10.1088/1361-6560/ab143f.

Assessment of histotripsy-induced liquefaction with diagnostic ultrasound and magnetic resonance imaging *in vitro* and *ex vivo*

Gregory J Anthony[1], **Viktor Bollen**[1], **Samuel Hendley**[1], **Tatjana Antic**[1], **Steffen Sammet**[1], **Kenneth B Bader**[1,2,3]

[1]The University of Chicago, Chicago, IL, United States of America

[2]Author to whom any correspondence should be addressed.

[3]K B is the senior author on this work.

Abstract

Histotripsy is a therapeutic ultrasound modality under development to liquefy tissue mechanically via bubble clouds. Image guidance of histotripsy requires both quantification of the bubble cloud activity and accurate delineation of the treatment zone. In this study, magnetic resonance (MR) and diagnostic ultrasound imaging were combined to assess histotripsy treatment *in vitro* and *ex vivo.* Mechanically ablative histotripsy pulses were applied to agarose phantoms or porcine livers. Bubble cloud emissions were monitored with passive cavitation imaging (PCI), and hyperechogenicity via plane wave imaging. Changes in the medium structure due to bubble activity were assessed with diagnostic ultrasound using conventional B-mode imaging and T_1-, T_2-, and diffusion-weighted MR images acquired at 3 Tesla. Liquefaction zones were correlated with diagnostic ultrasound and MR imaging via receiver operating characteristic (ROC) analysis and Dice similarity coefficient (DSC) analysis. Diagnostic ultrasound indicated strong bubble activity for all samples. Histotripsy-induced changes in sample structure were evident on conventional B-mode and T_2-weighted images for all samples, and were dependent on the sample type for T_1- and diffusion-weighted imaging. The greatest changes observed on conventional B-mode or MR imaging relative to baseline in the samples did not necessarily indicate the regions of strongest bubble activity. Areas under the ROC curve for predicting phantom or liver liquefaction were significantly greater than 0.5 for PCI power, plane wave and conventional B-mode grayscale, T_1, T_2, and ADC. The acoustic power mapped via PCI provided a better prediction of liquefaction than assessment of the liquefaction zone via conventional B-mode or MR imaging for all samples. The DSC values for T_2-weighted images were greater than those derived from conventional B-mode images. These results indicate diagnostic ultrasound and MR imaging provide complimentary sets of information, demonstrating that multimodal imaging is useful for assessment of histotripsy liquefaction.

Keywords

magnetic resonance imaging; passive cavitation imaging; diagnostic ultrasound; histotripsy

baderk@uchicago.edu.

Supplementary material for this article is available online

Introduction

Image-guided high intensity therapeutic ultrasound is a non-invasive modality for tissue ablation (Kennedy *et al* 2003, Kennedy 2005, Haar and Coussios 2007, Schulman *et al* 2017, Anthony *et al* 2019). Histotripsy is a form of focused ultrasound that ablates tissue via the nucleation and mechanical activity of bubble clouds, imparting lethal strain to target tissues (Parsons *et al* 2006, Roberts *et al* 2006, Khokhlova *et al* 2015, Bader *et al* 2019). Preclinical studies have applied histotripsy in the treatment of prostate tissue, liver and renal cancer, thrombosis, and stimulation of anti-tumor immune response (Khokhlova *et al* 2015). Additionally, a clinical trial was completed assessing the safety of histotripsy technology to treat benign prostatic hyperplasia (Schuster *et al* 2018).

Successful clinical implementation of histotripsy requires accurate and reliable image guidance to assess the treatment progress and efficacy. The presence of histotripsy-induced bubble activity and the resulting tis sue homogenization has been monitored with diagnostic ultrasound and magnetic resonance (MR) imaging (Hall *et al* 2005, Wang *et al* 2009, Kim *et al* 2013, 2014, Vlaisavljevich *et al* 2014, Allen *et al* 2017, Eranki *et al* 2017, Haworth *et al* 2017, Bader *et al* 2018a). Bubble clouds appear hyperechoic on B-mode imaging, and the strength of bubble cloud emissions can be mapped spatially with passive cavitation imaging (PCI) (Salgaonkar *et al* 2009, Gyöngy and Coussios 2010, Arvanitis and McDannold 2013, Arvanitis *et al* 2017, Crake *et al* 2017, Haworth *et al* 2017). Following histotripsy exposure, regions of tissue liquefaction can be assessed with B-mode imaging (Roberts 2014, Khokhlova *et al* 2015). A significant variability in the B-mode grayscale of ablation zones is observed between subjects, preventing quantification of the tissue liquefaction zone with B-mode imaging (Hall *et al* 2007, Zhang *et al* 2015). Diagnostic ultrasound is typically a 2D imaging modality, while MR imaging provides excellent soft tissue contrast over a volume with the potential for isotropic resolution (Kim *et al* 2013, 2014, Vlaisavljevich *et al* 2014, Allen *et al* 2017, Eranki *et al* 2017). Strong changes in MR contrast have been reported following histotripsy liquefaction (Kim *et al* 2013, 2014, Vlaisavljevich *et al* 2014, Eranki *et al* 2017). Combinations of diagnostic ultrasound and MR imaging have been implemented for thermal-based therapies (Arvanitis and McDannold 2013) and phase shift nanoemulsion-nucleated bubble activity during heating (Crake *et al* 2017), and may be an attractive multimodal option for histotripsy guidance.

The purpose of this study was to determine the relative utility of diagnostic ultrasound or MR imaging to predict histotripsy liquefaction. Histotripsy-induced bubble cloud activity was mapped with passive cavitation imaging (PCI) and plane wave imaging. Regions of liquefaction were visualized with conventional B-mode ultrasound and MR imaging. The relationship between histotripsy liquefaction and changes in MR or diagnostic ultrasound features were assessed quantitatively in agarose phantoms and *ex vivo* porcine liver.

Materials and methods

In vitro phantom preparation

Tissue mimicking agarose phantoms containing 15% v/v porcine red blood cell (RBC)/agarose layers were constructed following Maxwell *et al* (2010). Briefly, 50 mL of unspecified citrate-phosphate-dextrose porcine blood was obtained from a commercial vendor (Lampire Biological, Pipersville, PA, USA), and centrifuged at 3000 RPM for 10 min. The plasma and buffy coat supernatant were removed, leaving a pellet of RBCs. A 1% w/v agarose, 0.9% w/v NaCl (Sigma-Aldrich, St. Louis, MO, USA) solution was prepared using 0.2 μm filtered, deionized water and heated in a microwave at 700 W until clear. The agarose mixture was then transferred to a heated ultrasonic cleaning bath and degassed (50 kPa, 50% atmospheric pressure) for 30 min. After degassing, approximately 50 mL of the agarose mixture was poured into a custom acrylic mold ($6 \times 5 \times 5$ cm^3) with nylon wires embedded to serve as fiducial markers. After solidification of this layer, a layer of 15% v/v RBC/agarose mixture approximately 500 μm thick was pipetted onto the surface. This process was repeated to generate three RBC layers separated by 1.5 cm, after which the phantom was stored at 4 °C overnight (figure 1). Prior to histotripsy exposure, the phantoms were submerged in isotonic saline (0.9% NaCl w/v) and degassed (50 kPa pressure) for 2 h.

Phantom preparation with *ex vivo* liver samples

Porcine liver samples were collected from an abattoir and shipped fresh within 24 h via a commercial vendor (Lampire Biological, Pipersville, PA, USA), then cut to approximate dimensions of 6 cm × 3 cm × 1.5 cm. Liver samples were embedded in degassed, isotonic (0.9% NaCl w/v) 2% w/v low-gelling temperature agarose (product number A0701, Sigma-Aldrich, St. Louis, MO, USA) and stored at 4 °C overnight (figure 1). Prior to embedding the liver samples, the liquid agarose mixture was cooled to 40 °C. No thermal damage was evident upon histologic inspection of tissue samples. Prior to histotripsy exposure, the embedded samples were submerged in degassed isotonic saline (0.9% NaCl w/v) and degassed (50 kPa pressure) for 2 h.

Insonation and monitoring bubble activity

After degassing, phantoms were submerged in a tank of degassed (20% dissolved oxygen), filtered (10 μm pore size) water and affixed to a motor-controlled 3-axis positioning system (Thorlabs, Inc., Newton, NJ, USA) (figure 2). Histotripsy pulses were generated using a custom designed and built transducer and amplifier system (Hall *et al* 2006) (1 MHz center frequency, 90 mm focal length, 100 mm diameter, –6 dB focal zone dimensions: 10 mm × 2 mm × 2 mm). A total of 4000 pulses 5 μs in duration (Bader *et al* 2016b) were applied to each RBC layer with a pulse repetition frequency (PRF) of 100 Hz and peak negative pressures of 13, 17, 21, or 25 MPa. The peak negative pressures employed in this study span those previously used to successfully generate bubble activity via a shock-scattering mechanism (Maxwell *et al* 2013, Khokhlova *et al* 2015, Bader *et al* 2019). Exposure conditions were randomized for each RBC layer. During the insonation, bubble cloud acoustic emissions and hyperechogenicity generated by the bubble cloud were recorded with an L11–4v imaging array (Verasonics, Inc., Kirkland, WA, USA) using a research ultrasound scanner system (Vantage 128, Verasonics, Inc., Kirkland, WA, USA) triggered by the

histotripsy transmit electronics (Bader *et al* 2018a). Briefly, bubble cloud emissions were passively received over a 60 μs duration starting 5 μs prior to the 5 μs duration histotripsy pulse reaching the focus (figure 2(b)). Emissions were processed offline to generate passive cavitation images with a delay, sum, and integrate method in the frequency domain over the receive bandwidth of the imaging array (2–10 MHz) (Haworth *et al* 2017).

Bubble cloud hyperechogenicity is the primary method by which histotripsy therapy is guided (Hall *et al* 2007). Several milliseconds are required to execute the imaging sequence for conventional B-mode imaging, over which time the bubble cloud can undergo significant changes (Xu *et al* 2007, Maxwell *et al* 2011). Here, bubble cloud grayscale was assessed over a 20 μs window using plane wave imaging. To minimize constructive interference between the imaging and therapy pulses, the plane wave image was acquired 1 ms after the histotripsy focal insonation (Bader *et al* 2018a). During the 4000 applied pulses, plane wave images and cavitation emissions used to form passive cavitation images were acquired every tenth trigger pulse due to data transfer rate limitations (figure 2(b)), resulting in 400 frames per data set. In total, 33 insonations were performed in 11 different RBC phantoms.

Insonation and data acquisition for *ex vivo* liver samples were performed as described above, in three locations along the length of the sample (figure 1). A fixed peak negative pressure 25 MPa was employed to achieve consistent liquefaction. The peak negative pressure was derated to account for propagation through 1 cm of liver tissue with an attenuation coefficient of 0.32 dB cm^{-1} MHz^{-1} (Bader *et al* 2016a). To achieve consistent liquefaction in the liver samples, the total number of pulses was increased to 8000. In total, four liver samples were insonated, with three insonations per sample (12 total data sets).

Post hoc assessment of liquefaction: conventional B-mode and MR imaging

Image acquisition time relative to application of the histotripsy pulses is outlined in figure 2(b). Liquefied tissue appears as hypoechoic regions on conventional B-mode imaging (Hall *et al* 2007, Roberts 2014, Khokhlova *et al* 2015). For all samples, conventional B-mode images of the histotripsy target were acquired following the histotripsy insonation using the L11–4v imaging array to visualize the liquefaction zone. The purpose of these B-mode images was post hoc assessment of the histotripsy therapeutic efficacy. In contrast, plane wave images were employed to visualize the hyperechoic bubble cloud. The confluence of the hyperechoic bubble activity with hypoechoic changes in the material prevented assessment of the sample liquefaction during application of the histotripsy pulse. All samples were then imaged with a clinical 3 Tesla (3 T) MR scanner (Ingenia dStream, Philips Healthcare, Best, The Netherlands) using the body transmit coil and a 16-channel head-and-neck receive coil. Samples were submerged in Fomblin® (Solvay Specialty Polymers, Bollate, MI, Italy) during imaging to isolate the target signal from background and prevent parallel acquisition ghosting artifacts. Image slices were oriented parallel to the acoustic axis of the histotripsy source (azimuthal dimension of the diagnostic ultrasound imaging array, figure 2). The scan parameters for MR image acquisition are listed in table 1. Spin-echo (SE) and turbospin-echo (TSE) sequences were executed to acquire T_1- and T_2-weighted (T_1W and T_2W) images. Inversion-recovery (IR), multi-echo SE, and diffusion weighted imaging (DWI) sequences were utilized to quantify the relaxation times T_1 and T_2,

and the apparent diffusion coefficient (ADC) in the liquefaction zone. For the IR, multi-echo SE, and DWI sequences, the inversion time (TI), echo time (TE), and diffusion-weighting b-value were varied, respectively, across multiple acquisitions. From these sequences, T_1, T_2, and ADC were calculated on a voxel-by voxel basis by fitting magnitude image intensities to the following equations as a function of TI, TE, and b-value, respectively (Stejskal and Tanner 1965, Liney *et al* 1996, Fennessy *et al* 2012):

$$S = \left| S_0 \left(1 - 2e^{-\mathrm{TI}/T_1} + e^{-\mathrm{TR}/T_1} \right) \right|, \quad (1)$$

$$S = S_0 e^{-\mathrm{TE}/T_2}, \quad (2)$$

$$\ln(S) = \ln(S_0) - b\mathrm{ADC}, \quad (3)$$

where S is the signal amplitude of a magnitude image voxel, and S_0 is the fitted maximum signal amplitude as a function of TI, TE, or b-value. The parameters T_1, T_2, and ADC were estimated from least squares fits to equations (1)–(3) implemented with MATLAB software (MathWorks, Natick, MA, USA).

Image registration

Following MR scans, RBC phantoms were sectioned and photographed with a digital single-lens reflex (DSLR) camera (Nikon D3400, 24 MP resolution, Minato, Tokyo, Japan). Fiducial nylon wires embedded within the agarose gel were used to register optical phantom images, diagnostic ultrasound images, and MR images via a custom-scripted landmark-based affine registration implemented in MATLAB (Mathworks, Natick, MA,USA). Gross images were converted to grayscale and segmented using Otsu thresholding (Otsu 1979) to delineate regions of liquefied and intact phantom (figure 3).

Four-millimeter liver sections encompassing the liquefied regions were collected from each insonified region of the liver samples. Sections were fixed for 24–36 h in 10% buffered formalin (Sigma-Aldrich, St. Louis, MO, USA), transferred to 70% reagent alcohol (Thermo Scientific, Waltham, MA, USA) for 72 h, then processed and embedded in paraffin. Embedded tissues were sectioned at 5 μm thickness and stained with hematoxylin and eosin (H&E). Liver tissue slides were reviewed by a board-certified pathologist, who delineated the outer boundary of cellular necrosis as indicated by absence of nuclei and disruption of normal hepatic tissue structure. Minimal changes in tissue sample size occurred due to dehydration from histological processing.

Image analysis

The PCI power, plane wave (uncompressed) grayscale value, and changes in post hoc conventional B-mode (uncompressed) grayscale, T_1, T_2, and ADC from background were independently tested as quantitative predictors of RBC phantom liquefaction or liver tissue necrosis. The plane wave and conventional B-mode image grayscale pixel values are related to the backscattered acoustic power of the ultrasound imaging pulse (Radhakrishnan *et al* 2012). Post hoc conventional B-mode grayscale and T_2 exhibited both strong increases and decreases relative to background, and were assessed in terms of absolute change from the baseline signal. ROC curves were generated by varying a threshold across each ultrasound (acoustic power or plane wave/ conventional B-mode grayscale) and MR image quantity (T_1, T_2, or ADC) and plotting the true positive rate against false positive rate for prediction of liquefaction/necrosis at each threshold value (Metz 1978, Hanley and McNeil 1982). The delay, sum, and integrate beamforming algorithm used to form the passive cavitation images in this study is diffraction limited (Haworth *et al* 2017), causing emission artifacts along the range dimension for a linear imaging array (figures 2 and 5). Therefore, the ROC analysis was restricted to azimuthal pixels at a fixed range depth of 30 mm. A pixel was considered a true positive (false positive) when it was within the liquefaction zone of an RBC phantom or within the necrosis boundary of a liver sample and the quantitative image metric in question was greater than (less than) the threshold value. A pixel was considered a true negative (false negative) when it was within the intact area of an RBC phantom or outside the necrosis boundary of a liver sample and the quantitative image metric in question was less than (greater than) the threshold value. Areas under the receiver operating characteristic curve (AUCs) were calculated for each quantitative image metric for RBC phantoms and liver samples. The optimal point along the curve, indicative of a threshold value for phantom liquefaction, was identified following Hanley and McNeil (1982). The sensitivity, specificity, accuracy, and positive and negative predictive values (PPV and NPV) at this threshold point were calculated via:

$$\text{Sensitivity} = \frac{\text{TP}}{\text{TP+FN}}, \quad (4)$$

$$\text{Specificity} = \frac{\text{TN}}{\text{TN+FP}}, \quad (5)$$

$$\text{Accuracy} = \text{Sensitivity} \cdot P + \text{Specificity} \cdot (1 - P), \quad (6)$$

$$\text{PPV} = \frac{\text{TP}}{\text{TP+FP}}, \quad (7)$$

$$\mathrm{NPV} = \frac{\mathrm{TN}}{\mathrm{TN+FN}}, \quad (8)$$

where TP and TN are the true positive and true negative rate, respectively, FP and FN are the false positive and false negative rate, respectively, and P is the overall prevalence of liquefaction/necrosis, or the percentage of azimuthal pixels across all RBC phantoms/liver samples that are within the liquefaction/necrosis zone. Confidence intervals for ROC curves were obtained via bootstrap resampling with 1000 iterations to test the significance of the AUC relative to random guessing (AUC = 0.5). Significant differences in the above statistics between ROC curves were assessed according to DeLong *et al* (1988).

The Dice similarity coefficient (DSC) was employed to quantify post hoc conventional B-mode and T_2W imaging assessment of the liquefaction zone (Crum *et al* 2006). Diffusion-weighted and T_1W images were excluded from the DSC analysis, as liquefaction zones were not consistently apparent with these modalities. Passive cavitation and plane wave images acquired during the histotripsy insonation track bubble activity, and are therefore not a direct means to assess the ablation zone. DSC values were computed as:

$$\mathrm{DSC} = \frac{2(A \cap B)}{(A + B)}, \quad (9)$$

where $(A \cap B)$ is the area of the intersection of an image-derived liquefaction zone and the true liquefaction zone, and $(A + B)$ is the sum of these two areas. For RBC phantoms and liver samples, DSC values derived from conventional B-mode and $T2W$ images were compared at each pressure level using paired Student's t-tests. For RBC phantoms, DSC values for 13, 17, 21, and 25 MPa insonations were compared separately using one-way unbalanced analysis of variance (ANOVA) and Tukey's honestly significant difference (HSD) as a post hoc test. Differences in the areas of RBC phantom liquefaction zones as measured from gross observation images were also compared between all pressures using one-way unbalanced ANOVA and Tukey's HSD. All statistical analysis was performed with an α level of 0.05.

Features of diagnostic ultrasound and MR images were also evaluated without comparison to gross observations of histotripsy liquefaction. The azimuthal locations of maximum PCI power, plane wave grayscale, $T1$, and ADC, and the maximum and minimum post hoc conventional B-mode grayscale and T_2 relative to the geometric transducer focus were recorded for each RBC phantom data set. Background ROIs were also drawn for each sample in untargeted portions of RBC layers or liver tissue, and the average PCI acoustic power, plane wave and post hoc conventional B-mode grayscale, T_1, T_2, and ADC values within the liquefaction zones and background ROIs were computed. Differences in image parameters between liquefaction zones and background were evaluated using paired Student's t-tests. For RBC phantoms, differences in image parameters between pressures were assessed using one-way unbalanced ANOVA with Tukey's HSD as a post hoc test. All statistical analysis was performed with an α level of 0.05.

Results

Observation of histotripsy-induced liquefaction

Liquefaction occurred within RBC phantoms at all pressures. For six of eight 13 MPa insonations, ‘streaks’ of inhomogeneous liquefaction were observed at the distal end of the focal zone. As the pressure increased, the liquefaction zone transitioned from a ‘tadpole’ shape to being semi-conical with a wide, flattened head (figure 4, top row). The measured liquefaction area increased significantly with the peak negative pressure of the histotripsy pulse. Targeted areas in liver samples exhibited extensive denucleation and homogenization of cellular membranes and tissue structure that was most pronounced at the head of the liquefaction zone (figures 7(a), 8(a), and 10(b)). The outer boundary of observed denucleation (necrosis) was assessed, although some areas of nucleated cells were still present in this region.

Monitoring bubble activity with PCI/plane-wave imaging

Table 2 displays bubble-monitoring and post-insonation image parameter values measured within liquefaction zones for all phantom and tissue samples. Bubble clouds were generated in all samples for all insonations as indicated by hyperechogenicity on plane wave images and strong acoustic emissions on passive cavitation images (figures 5 and 6). Good correspondence was observed between locations of bubble activity, highlighted by hyperechogenicity on plane wave imaging and acoustic emissions on PCI, and histotripsy liquefaction observed in post hoc conventional B-mode and T_2W images (figures 4 and 5). RBC phantom liquefaction zones, defined as regions void of red blood cells, were determined using Otsu thresholding (Otsu 1979) (see ‘Image Registration’ in Methods section and figure 3). The PCI power of acoustic emissions within the RBC phantom liquefaction zones increased significantly at each pressure level, while plane wave grayscale values tracking the hyperechoic bubble cloud within liquefaction zones only increased significantly between 13 and 17 MPa insonations. Bubble cloud activity quantified by acoustic power and grayscale within the liquefaction zones were significantly greater than background values for all phantom and tissue samples. For all RBC phantoms (figure 6) and most liver samples (figure 7), bubble activity appeared continuously throughout the focal zone. In four of 12 liver samples, bubble activity occurred preferentially along connective, vascular, or ductal structures.

Post hoc conventional B-mode imaging: RBC phantoms

Hypoechoic regions were observed in post-insonation conventional B-mode images of RBC phantoms, corresponding to the liquefaction zone (figure 4, middle row). In 15 of 33 cases, a rim of hyperechoic signal was visible surrounding the hypoechoic region. The intensity of this rim tended to increase with distance from the histotripsy source and increase with peak negative pressure. Due to this rim feature and highly variable echogenicity, no significant differences in conventional B-mode grayscale were observed between liquefaction zones and background areas at any pressure level.

Post hoc conventional B-mode imaging: liver samples

Hypoechoic lesions were apparent following insonation of liver samples, although eight of 12 lesions also contained small hyperechoic structures throughout (figure 8(b)). No significant difference in conventional B-mode grayscale between liquefaction zones and background was observed in liver samples.

Post hoc 3 T MRI of RBC phantoms

Figure 9 depicts quantitative maps of T_1, T_2, and ADC from a typical RBC phantom. In all RBC phantoms, there was qualitative agreement in the features of T_1W or T_2W images and quantitative T_1 or T_2 maps. Changes in T_1 and absolute changes in T_2 relative to background were significantly greater than zero for all peak negative pressures. A significant increase in ADC from background was observed for 17 and 25 MPa insonations only. Values of T_1, T_2, and ADC measured within liquefaction zones did not change significantly between pressure levels.

Post hoc 3 T MRI of liver samples

Areas of liquefaction in liver samples were clearly demarcated in post hoc T_2W MR images (figure 8(c)). Liquefaction zones of liver samples exhibited significant increases in T_2 and ADC of 7.2 ± 1.8 ms and 0.34 ± 0.10 mm^2 ms^{-1}, respectively. No significant T_1 changes were observed in liver samples after histotripsy exposure.

Image analysis/spatial correlation of red blood cell phantoms

Good qualitative agreement was observed between the visualized red blood cell liquefaction zone, observations of bubble activity via acoustic emissions and hyperechogenity, and visualized changes in the phantom structure (figures 4 and 6). For peak negative pressures of 17 MPa or less, azimuthal locations of peak PCI power and peak plane wave grayscale were typically coincident with each other and proximal to the geometric focus of the histotripsy source (figures 10(a) and 11). As peak negative pressure of the histotripsy pulse increased, a second peak in the plane wave grayscale was observed near the geometric focus of the therapy source (figures 10(b) and 11). Parametric MR images of the liquefaction zone indicated that the areas of greatest change in the relaxation time T_2 corresponded to areas of relatively low PCI power and plane wave grayscale value (figure 10(a)). At peak negative pressures greater than 13 MPa, liquefaction zones exhibited a spatially-varying T_2 signature: T_2 increased maximally at the head of the liquefaction zone and tended to decrease below background level at the tail (figures 10(a) and 11). T_1 and ADC did not exhibit a preferential location of greatest change within phantom liquefaction zones.

Bubble activity and ablation were elongated along the azimuthal dimension compared with the range dimension. Good correspondence between locations of liquefaction and imaging features were observed along the range dimension (figure S2 (stacks.iop.org/PMB/64/095023/mmedia)). However, the limited range resolution of the delay, sum, and integrate beamformer prevented meaningful analysis of the passive cavitation images along this dimension (Haworth *et al* 2017).

Image analysis/spatial correlation of liver samples

Areas of liver qualified pathologically as necrotic (area within dotted outline in figures 7(a) and 10(b)) corresponded spatially to locations of elevated PCI power, plane wave grayscale, T_2, and ADC (figures 7 and 10(b)). The greatest sources of PCI emissions coincided with locations of greatest denucleation as indicated by histology (figures 7(a)–(c) and 10(b)). A second local maximum in both the PCI power and plane wave grayscale distal to the peak emission location was present in 11 of 12 liver samples (figure 10(b)). Peak plane wave grayscale values were located near the geometric focus, while T_2 and ADC maxima were typically proximal, also coinciding with the most thoroughly liquefied areas and regions of strong bubble cloud acoustic emissions (figures 7(d)–(i) and 10(b)). Figure S2(b) depicts profiles of PCI power, plane wave grayscale, and change in T_2 along the range dimension of a liver sample.

Receiver operating characteristic (ROC) analyses

The ROC curves obtained from comparing quantitative imaging features to histotripsy-induced liquefaction are shown in figure 12. The AUC values, thresholds for phantom liquefaction/liver necrosis, and the sensitivity, specificity, and accuracy at these threshold values are reported in tables 3 and 4. For liver samples and RBC phantoms, confidence intervals of ROC curves indicated that all diagnostic ultrasound and MR image parameters resulted in AUCs significantly greater than 0.5, indicating improved performance over guessing.

ROC analysis: RBC phantoms

For all image parameters, no trend in RBC phantom AUC was apparent with increasing pressure level. Assessment of bubble activity via plane wave imaging or PCI performed significantly better than post hoc assessment of the liquefaction zone with MR or conventional B-mode imaging. T_1 performed significantly better than T_2, which performed significantly better than ADC and post hoc conventional B-mode grayscale. At the optimal discrimination thresholds, specificity was greater than 0.84 for all image parameters. T_1 was more sensitive to liquefaction than T_2, whereas T_2 was more specific to liquefaction. Due to the low discriminatory power of ADC, its threshold resulted in 100% negative classifications and an undefined positive predictive value. Similarly, post hoc conventional B-mode exhibited low discriminatory power and a threshold strongly favoring negative classification. Excluding ADC, sensitivity was lowest for post hoc conventional B-mode compared with all other diagnostic ultrasound and MR imaging parameters.

ROC analysis: liver samples

All image parameters from liver samples resulted in significantly different AUC values. PCI power performed best, followed by ADC, plane wave grayscale, T_2, T_1, and post hoc conventional B-mode grayscale. At the optimal discrimination thresholds, PCI power and plane wave grayscale were more sensitive to liquefaction than any MR image parameter, although all three MR parameters were significantly more specific to liquefaction than plane wave grayscale. Compared with plane wave grayscale, ADC and T_2 also had significantly

improved PPV, and ADC had significantly improved accuracy. Post hoc conventional B-mode grayscale had the lowest AUC value, but was more sensitive to liquefaction than T_1.

Dice Similarity Coefficient Analysis

Dice Similarity Coefficient (DSC) values derived from post hoc conventional B-mode images and T_2W images are given in table 5. In RBC phantoms, with the exception of 17 MPa peak negative pressure pulses, DSC values were significantly greater for T_2W images than post hoc conventional B-mode images. For peak negative pressures of 17, 21, and 25 MPa, DSC values were significantly higher than 13 MPa insonations for both post hoc conventional B-mode and T_2W images. In liver samples, DSC values derived from T_2W image outlines were significantly greater than those derived from conventional B-mode image outlines.

Discussion

Observations of phantom/tissue liquefaction

Liquefaction was achieved in all phantom and tissue samples for all pressures utilized in this study. In RBC phantoms, the lesion morphology and area were dependent on the peak negative pressure of the histotripsy pulse. Liquefaction within the head of the treatment zone appeared continuous. Discontinuous regions of liquefaction at the tail of the focal zone were occasionally present near the periphery (figure S3). Areas of residual nucleated cells were also found in liver necrosis zones, alongside sites of apparent preferential cavitation. These observations are consistent with descriptions of cavitation memory effects, in which the application of histotripsy pulses at pulse repetition frequencies greater than 1–10 Hz increases the spatial persistence of bubble clouds (Huber *et al* 1999, Wang *et al* 2012, Shi *et al* 2018). Bubble cloud persistence generates mechanical activity at finite spatial locations within the focal zone and may result in inhomogeneous liquefaction. Applying histotripsy pulses at a lower repetition frequency or applying bubble-deleting pulses (Alavi Tamaddoni *et al* 2016) between therapeutic pulses would improve liquefaction zone uniformity. Residual regions within liquefaction zones may also be reflective of stiff tissue structures resistant to the lethal strain induced by the bubble cloud activity (Vlaisavljevich *et al* 2014).

Prediction of liquefaction via bubble activity

One primary consideration for all image-guided therapies is to establish a quantitative, image-based dose metric with which to control the application of therapy. PCI provides a quantitative measure of the strength of histotripsy bubble cloud activity (Haworth *et al* 2017). A key result of this study is that observations of bubble activity were better indicators of liquefaction than post hoc assessment via conventional B-mode or MR imaging (figure 12). Prediction of RBC phantom liquefaction was similar for PCI and plane wave grayscale, whereas PCI provided an improved prediction of liver sample liquefaction compared with plane wave imaging. The liver samples have an increased acoustic attenuation compared with the agarose phantoms, which may account for the discrepancy in liquefaction prediction between PCI and plane wave imaging. In a similar study, PCI provided an improved prediction of histotripsy liquefaction compared with plane wave imaging in an attenuating prostate tissue phantom (Bader *et al* 2018a). The significantly reduced specificity

of plane wave imaging in the liver samples of this study also suggests a greater incidence of false positives from highly reflective structures in the tissue. There may be other reasons for the similar predictive power of PCI and plane wave imaging observed in RBC phantoms. The study presented here utilized a pulse repetition frequency five times larger than the prostate phantom study (100 versus 20 Hz), which may have increased bubble cloud persistence spatially and improved the correlation between plane wave grayscale and phantom liquefaction. The total number of pulses applied in this study was also increased by a factor of 2 (4000 versus 2000), which would reduce noise in the averaged data.

Post hoc evaluation of liquefaction with MR and conventional B-mode imaging

Accurate assessment of the liquefaction zone extent is necessary to confirm histotripsy treatment efficacy. Insonation of liver tissue samples in this study resulted in more pronounced and uniform changes in T_1, T_2, and diffusion compared with RBC phantoms. Uniform increases in T_2 and ADC and both uniform increases and decreases in T_1 have been observed previously following boiling histotripsy ablation in *ex vivo* tissue (Eranki *et al* 2017, Partanen *et al* 2014). Allen *et al* (2017) reported uniform increases in T_1, T_2 and ADC in similar 16% RBC phantoms and *ex vivo* tissue samples following histotripsy liquefaction, but utilized 2-cycle pulses from a 400 kHz transducer with a 10 Hz PRF. In contrast, this study utilized shock-scattering histotripsy pulses of 5-cycle duration from a 1 MHz source at a PRF of 100 Hz. Allen *et al* (2017) acquired MR images of histotripsy ablation, where the focus of the source was rastered throughout a volume. Here, in contrast, histotripsy pulses were applied to a single fixed location. The MR image slices in this study were oriented parallel to the direction of ultrasound propagation to observe variations in the liquefaction zone along this axial dimension. Allen *et al* (2017) oriented MR image slices perpendicular to the direction of ultrasound propagation, which would likely homogenize the appearance of the ablation zone.

In this study, MR image slices of RBC phantoms encompassed both pure agarose and thin RBC layers. Therefore, only a portion of MR signal originated from the RBC layers, degrading the contrast between liquefied and intact structures. Following histotripsy, homogenization of paramagnetic blood agents is the primary source of change in T_2, while disruption of diffusion-limiting membranes tends to increase apparent diffusion (Allen *et al* 2017). The greater density of red blood cells and cell/nuclear membranes in tissue samples likely made liquefaction more evident. Indeed, much stronger changes in T_1, T_2, and ADC following histotripsy liquefaction were observed in human whole blood clots in comparison to the red blood cell phantoms (figure S1, tables S1 and S2). Histological lesion boundaries in liver samples were based on denucleation and homogenization of cellular structures, rather than red blood cell lysis, which may explain the improved discriminatory power of ADC over $T2$ observed in liver samples.

Reduction in B-mode image backscatter is the primary method for evaluating the efficacy of histotripsy therapy in pre-clinical studies (Hall *et al* 2007) and was employed in a clinical trial assessing histotripsy ablation of the prostate (Schuster *et al* 2018). Hypoechoic regions in B-mode images have been shown to correlate with histologic areas of liquefaction (Roberts 2014, Khokhlova *et al* 2015). In this study, the information provided by

conventional B-mode imaging was limited due to low contrast-to-noise ratios between intact and liquefied tissue, image artifacts, and hyperechoic structures within and surrounding liquefaction zones (figures 4 and 8(b)). Post hoc conventional B-mode imaging produced the lowest AUC of any image parameter studied and exhibited worse correlation with liquefaction and lesion morphology than T_2W images for both RBC phantoms and liver samples. While T_2 maps of liquefied RBC layers exhibited spatially varying features (figures 6(d)–(f)), liquefaction zones were easily identified in liver samples by a marked increase in intensity (figures 7(d)–(f)). Previous studies have demonstrated strong agreement of morphology between T_2W imaging and gross histologic observation of histotripsy lesions, suggesting this image modality is well suited to evaluation of histotripsy ablation (Kim *et al* 2013, Vlaisavljevich *et al* 2014). The liquefaction zone for RBC phantoms tended to be underestimated by conventional B-mode imaging (26 of 33 insonations) but overestimated by T_2W MR imaging (18 of 33 insonations). Both imaging modalities underestimated histologic lesion areas for liver samples, but T_2W image outlines more closely approximated necrosis boundaries. Post hoc evaluative imaging, particularly MRI, may be a necessary supplement to bubble-monitoring techniques for histotripsy guidance.

Relationship between diagnostic ultrasound, MRI, and liquefaction

Diagnostic ultrasound and MR imaging can provide complimentary data to inform histotripsy guidance. The short timescale of bubble cloud activity is best captured with the real-time capability of diagnostic ultrasound imaging, while MR image contrast can supply clearer delineations of the liquefaction zone post-insonation. In this study, the information provided by each image modality varied between tissue and RBC phantom samples, most notably as the predictive power of MR imaging improved considerably in liver samples. The intersection of ROC curves for plane wave grayscale, T_2, and ADC measured from liver samples in this study (figure 12(b)) suggest that constructing a liquefaction classifier based on input from more than one of these image modalities (e.g. logistic regression) (Cox 1958) would improve classification of liquefied and intact tissue. Such a multi-modal approach to histotripsy image guidance could improve accuracy of treatment zone measurements and improve treatment outcomes. Although PCI produced greater AUC values than any other image metric, its limited range resolution necessitates the use of supplementary image data (e.g. plane wave, conventional B-mode, or MRI) to predict two-and three-dimensional liquefaction zones. In the RBC phantoms, fewer of the analyzed pixels were associated with liquefaction compared with intact structure (30% liquefied and 70% intact). As a result, the liquefaction threshold pixel value for weaker discriminators of liquefaction (e.g. conventional B-mode grayscale, T_2, and ADC) favored specificity over sensitivity (table 3). These modalities would therefore not provide good sensitivity to the onset of tissue liquefaction. The use of absolute changes in T_2 and post hoc conventional B-mode grayscale from background also likely reduced the power of these features in distinguishing liquefaction in this study, as both positive and negative fluctuations in noise masked the liquefaction-induced changes.

In all materials studied, the azimuthal locations of maximum changes in diagnostic ultrasound and MR image parameters appeared to reflect the evolution of the bubble cloud and resulting liquefaction. In RBC phantoms, the location of strongest bubble cloud activity

as indicated by PCI was consistently at the proximal, wider end of the lesion. The observation of two plane wave grayscale peaks in this study was also reported by Bader *et al* (2018a) during histotripsy insonation of prostate-mimicking phantoms. This phenomenon likely reflects nuclei expansion at the focal zone as well as strong bubble activity induced by shock scattering of incident waves proximal to the source (Maxwell *et al* 2011). For peak negative pressures of 25 MPa, the intensity of the distal plane wave peak surpassed that of the proximal peak and was accompanied by the appearance of a second PCI peak (figure 10(b)). The distal peak at the geometric focus of the therapy source likely indicates onset of intrinsic threshold cavitation (Maxwell *et al* 2013, Lin *et al* 2014, Bader *et al* 2019) in addition to proximal shock-scattering cavitation. In RBC phantoms, the observed maxima and minima in T_2 became increasingly separated with increasing pressure (figure 11). Decreases in T_2 at the tail ends of RBC phantom liquefaction zones may indicate distal accumulation of agarose debris and paramagnetic blood agents due to streaming, which was also suggested by hyperechoic tails in the post hoc conventional B-mode images. These features were more pronounced at greater peak negative pressures and may be due to intense streaming from the bubble cloud that causes accumulation of debris at certain locations within the liquefaction zone over time. The onset of such streaming may indicate the area was liquefied over the course of many applied pulses, suggesting overtreatment. The maximum observed increases in T_2 at the proximal edge and around the liquefaction boundary are likely due to the magnetic susceptibility difference between the intact and liquefied agar matrix. In liver samples, a spatial variation in T_2 and ADC was also present in 3 of 12 lesions (figures 7(d)–(i)). Maxima for both of these parameters were frequently located at the proximal end of liver necrosis zones. Furthermore, histological liver slides indicated liquefaction was most thorough at the proximal ends of the lesions, which also exhibited peaks in PCI and plane wave grayscale intensity. These findings collectively indicate that both diagnostic ultrasound and MR image features could potentially quantify the efficacy of histotripsy liquefaction, which may vary along the axial dimension for certain insonation parameters. Furthermore, combining PCI and plane wave image data can indicate which histotripsy modes (e.g. shock-scattering versus intrinsic threshold) are occurring.

Limitations

There are some aspects of this study that limit the generalizability of the findings. The ROC and DSC analyses of liver samples in this study were limited due to some distortion of the tissue and lesion morphology during histological processing. The ROC analysis was based on a binary model of treatment outcome (i.e. intact or liquefied), which may oversimplify the liquefaction process. Future studies should explore the type of cell death or *in vivo* immunological response relative to imaging features. The histotripsy insonation parameters could also be varied to determine sensitivity of the image parameters explored here to varying degrees of histotripsy liquefaction. The objective of this study was to determine the accuracy of diagnostic ultrasound and MR image quantities in predicting spatial locations of histotripsy liquefaction. Therefore, the histotripsy insonation parameters were chosen such that liquefaction occurred somewhere within the imaging plane, but not everywhere throughout the entire imaging plane. Including samples without any observable liquefaction may produce a more robust analysis.

The findings of this study constitute a post hoc analysis of histotripsy liquefaction, and were not tested as a real-time prediction of liquefaction. The optimal operating points extracted from the ROC curves provide quantitative pixel values associated with liquefaction, but may vary based on the tissue type, array sensitivity, or the therapy insonation conditions. Conclusions of the ROC analysis were restricted to the azimuthal dimension due to the limited range resolution of PCI. Histotripsy bubble activity is strongest along the central axis of the therapy source (azimuthal dimension for this study, figure 2) (Maxwell *et al* 2011). Alternative beamforming algorithms can be implemented to reduce the range artifact, but have an increased computational load for image generation (Stoica *et al* 2003, Coviello *et al* 2015). Alternatively, sparse, multi-element detectors can be constructed with favorable point spread functions to minimize the artifact (O' Reilly *et al* 2014).

In this study, passive cavitation and plane wave images were analyzed based on a pixel-by-pixel summation of all frames acquired for a given data set (400 frames per data set for RBC phantoms, 800 frames per data set for liver samples). The temporal averaging of the images used here neglects changes in the bubble activity as the medium liquefies (Zhang *et al* 2015, Macoskey *et al* 2018a, 2018b). The use of MR parameter changes to evaluate liquefaction as presented here also constitutes only a post hoc assessment, rather than real-time monitoring of treatment. Other studies have assessed MR cavitation contrast for monitoring the mechanical action of histo-tripsy (Allen *et al* 2015, 2016) and MR thermometry for monitoring tissue boiling at pre-clinical field strengths (4.7–9 T) (Khokhlova *et al* 2009). In this study, MR images were acquired with a 3 T clinical scanner.

The phantoms and tissue samples evaluated in this study may not be representative of histotripsy liquefaction *in vivo.* The liquefaction zone was visualized in this study at a fixed time point shortly following the histotripsy exposure, which does not capture changes in the lesion morphology over the course of the applied pulses. Physiologic responses due to the therapeutic insonation may obfuscate the ablation extent in post hoc evaluative imaging immediately following treatment (Partanen *et al* 2013, Zhou 2011). In particular, the use of T_2W imaging to designate histotripsy ablation may be complicated *in vivo* by the presence of hemorrhage and lesion evolution (Vlaisavljevich *et al* 2016). The appearance of post hoc images following histotripsy may therefore be highly dependent on the timing of their acquisition, underscoring the importance of real-time monitoring of bubble cloud activity via PCI for successful histotripsy guidance. However, the utility of MR imaging in detecting liquefaction-induced tissue changes and delineating histotripsy lesions has been demonstrated both in prior studies (Kim *et al* 2013, 2014, Vlaisavljevich *et al* 2014, Allen *et al* 2017, Eranki *et al* 2017) and the ROC and DSC analysis of this study. This suggests a multi-modal image guidance scheme including PCI and plane wave imaging for monitoring cavitation and MR imaging for lesion assessment may be well-suited to histotripsy ablation and facilitate its clinical translation. Advancing analysis techniques such as machine learning that delineate the extent of damage in post hoc imaging may also aid in the assessment of histotripsy treatment progress (Sahiner *et al* 2019).

Conclusion

This *in vitro* and *ex vivo* study examined the relative utility of diagnostic ultrasound and MR imaging for predicting histotripsy-induced liquefaction. In red blood cell phantoms, quantitative measurements of ultrasound passive cavitation imaging (PCI) power, ultrasound plane wave grayscale, and magnetic resonance (MR) imaging T_1 and T_2 relaxation times were indicative of histotripsy induced cavitation activity and resultant liquefaction. Changes in MR imaging parameters post-histotripsy were most apparent in tissue samples. Post hoc conventional B-mode imaging proved to be an unreliable indicator of liquefaction compared with other diagnostic ultrasound and MR imaging parameters. PCI power produced the largest area under the curve for all materials studied, but the performances of PCI, plane wave, and MR modalities were more comparable in liver samples. Delineation of lesions from T_2-weighted images more accurately reflected phantom and tissue liquefaction than post hoc conventional B-mode images. The use of multiple imaging modalities provides complimentary information and improves the assessment of histotripsy liquefaction compared with current clinically-used approaches.

Supplementary Material

Refer to Web version on PubMed Central for supplementary material.

Acknowledgments

We would like to acknowledge and thank the MRIRC research core and the HTRC core facility for their support on this project. This work was supported in part by the National Institutes of Health Grant R01HL133334, Grant K12CA139160, and Grant T32EB002103 (Greg Anthony), the University of Chicago Comprehensive Cancer Center and National Institutes of Health National Cancer Institute under Grant P30CA014599, and the Paul C Hodges Alumni Society of the Department of Radiology at the University of Chicago.

References

Alavi Tamaddoni H, Roberts WW, Duryea AP, Cain CA and Hall TL 2016 Enhanced high-rate shockwave lithotripsy stone comminution in an *in vivo* porcine model using acoustic bubble coalescence J. Endourol 30 1321–5 [PubMed: 27762629]

Allen SP, Hall TL, Cain CA and Hernandez-Garcia L 2015 Controlling cavitation-based image contrast in focused ultrasound histotripsy surgery Magn. Reson. Med 73 204–13 [PubMed: 24469922]

Allen SP, Hernandez-Garcia L, Cain CA and Hall TL 2016 MR-based detection of individual histotripsy bubble clouds formed in tissues and phantoms Magn. Reson. Med 76 1486–93 [PubMed: 26599823]

Allen SP, Vlaisavljevich E, Shi J, Hernandez-Garcia L, Cain CA, Xu Z and Hall TL 2017 The response of MRI contrast parameters in *in vitro* tissues and tissue mimicking phantoms to fractionation by histotripsy Phys. Med. Biol 62 7167 [PubMed: 28741596]

Anthony GJ et al. 2019 MRI-guided transurethral insonation of silica-shell phase-shift emulsions in the prostate with an advanced navigation platform Med. Phys 46 774–88 [PubMed: 30414276]

Arvanitis CD and McDannold N 2013 Integrated ultrasound and magnetic resonance imaging for simultaneous temperature and cavitation monitoring during focused ultrasound therapies Med. Phys 40 112901 [PubMed: 24320468]

Arvanitis C, Crake C, McDannold N and Clement G 2017 Passive acoustic mapping with the angular spectrum method *IEEE Trans*. Med. Imaging 36 983–93

Bader KB, Crowe MJ, Raymond JL and Holland CK 2016a Effect of frequency-dependent attenuation on predicted histotripsy waveforms in tissue-mimicking phantoms Ultrasound Med. Biol 42 1701–5 [PubMed: 27108036]

Bader KB, Haworth KJ, Maxwell AD and Holland CK 2018a Post hoc analysis of passive cavitation imaging for classification of histotripsy-induced liquefaction *in vitro IEEE Trans*. Med. Imaging 37 106–15

Bader KB, Haworth KJ, Shekhar H, Maxwell AD, Peng T, McPherson DD and Holland CK 2016b Efficacy of histotripsy combined with *rt-PA in vitro* Phys. Med. Biol 61 5253 [PubMed: 27353199]

Bader KB, Vlaisavljevich E and Maxwell AD 2019 For whom the bubble grows: physical principles of bubble nucleation and dynamics in histotripsy ultrasound therapy Ultrasound Med. Biol 45 1056–80 [PubMed: 30922619]

Coviello C, Kozick R, Choi J, Gyongy M, Jensen C, Smith PP and Coussios C-C 2015 Passive acoustic mapping utilizing optimal beamforming in ultrasound therapy monitoring J. Acoust. Soc. Am 137 2573–85 [PubMed: 25994690]

Cox DR 1958 The regression analysis of binary sequences J. R. Stat. Soc. B 20 215–42

Crake C, Meral FC, Burgess MT, Papademetriou IT, McDannold NJ and Porter TM 2017 Combined passive acoustic mapping and magnetic resonance thermometry for monitoring phase-shift nanoemulsion enhanced focused ultrasound therapy Phys. Med. Biol 62 6144–63 [PubMed: 28590938]

Crum WR, Camara O and Hill DLG 2006 Generalized overlap measures for evaluation and validation in medical image analysis *IEEE Trans*. Med. Imaging 25 1451–61

DeLong ER, DeLong DM and Clarke-Pearson DL 1988 Comparing the areas under two or more correlated receiver operating characteristic curves: a nonparametric approach Biometrics 44 837–45 [PubMed: 3203132]

Eranki A. et al. 2017; Boiling histotripsy lesion characterization on a clinical magnetic resonance imaging-guided high intensity focused ultrasound system. PLOS One. 12:e0173867. [PubMed: 28301597]

Fennessy FM, Fedorov A, Gupta SN, Schmidt EJ, Tempany CM and Mulkern RV 2012 QIN: practical considerations in T1 mapping of prostate for dynamic contrast enhancement pharmacokinetic analyses Magn. Reson. Imaging 30 1224–33 [PubMed: 22898681]

Gyongy M and Coussios CC 2010 Passive spatial mapping of inertial cavitation during HIFU exposure IEEE Trans. Biomed. Eng 57 48–56 [PubMed: 19628450]

Haar DGT and Coussios C 2007 High intensity focused ultrasound: physical principles and devices Int. J. Hypertherm 23 89–104

Hall TL, Fowlkes JB and Cain CA 2005 Imaging feedback of tissue liquefaction (histotripsy) in ultrasound surgery IEEE Ultrasonics Symposium, 2005 vol 3, pp 1732–4

Hall TL, Fowlkes JB and Cain CA 2007 A real-time measure of cavitation induced tissue disruption by ultrasound imaging backscatter reduction *IEEE Trans*. Ultrason. Ferroelectr. Freq. Control 54 569–75

Hall T, Cain C, Clement GT, McDannold NJ and Hynynen K 2006 A low cost compact 512 channel therapeutic ultrasound system for transcutaneous ultrasound surgery AIP Conf. Proc. 829 445–9

Hanley JA and McNeil BJ 1982 The meaning and use of the area under a receiver operating characteristic (ROC) curve Radiology 143 29–36 [PubMed: 7063747]

Haworth KJ, Bader KB, Rich KT, Holland CK and Mast TD 2017 Quantitative frequency-domain passive cavitation imaging *IEEE Trans*. Ultrason. Ferroelectr. Freq. Control 64 177–91

Huber P, Debus J, Jochle K, Simiantonakis I, Jenne J, Rastert R, Julia S, Lorenz WJ and Wannenmacher M 1999 Control of cavitation activity by different shockwave pulsing regimes Phys. Med. Biol 44 1427 [PubMed: 10498515]

Kennedy JE 2005 High-intensity focused ultrasound in the treatment of solid tumours Nat. Rev. Cancer 5 321–7 [PubMed: 15776004]

Kennedy JE, ter Haar GR and Cranston D 2003 High intensity focused ultrasound: surgery of the future? Br. J. Radiol 76 590–9 [PubMed: 14500272]

Khokhlova TD, Canney MS, Lee D, Marro KI, Crum LA, Khokhlova VA and Bailey MR 2009 Magnetic resonance imaging of boiling induced by high intensity focused ultrasound. J Acoust. Soc. Am 125 2420–31 [PubMed: 19354416]

Khokhlova V, Fowlkes J, Roberts W, Schade G, Xu Z, Khokhlova T, Hall T, Maxwell A, Wang Y and Cain C 2015 Histotripsy methods in mechanical disintegration of tissue: toward clinical applications Int. J. Hypertherm 31 145–62

Kim Y, Fifer CG, Gelehrter SK, Owens GE, Berman DR, Vlaisavljevich E, Allen SP, Ladino-Torres MF and Xu Z 2013 Developmental impact and lesion maturation of histotripsy-mediated non-invasive tissue ablation in a fetal sheep model Ultrasound Med. Biol 39 1047–55 [PubMed: 23453378]

Kim Y, Vlaisavljevich E, Owens GE, Allen SP, Cain CA and Xu Z 2014 *In vivo* transcostal histotripsy therapy without aberration correction Phys. Med. Biol 59 2553 [PubMed: 24785433]

Lin K-W, Kim Y, Maxwell AD, Wang T-Y, Hall TL, Xu Z, Fowlkes JB and Cain CA 2014 Histotripsy beyond the intrinsic cavitation threshold using very short ultrasound pulses: microtripsy IEEE Trans. Ultrason. Ferroelectr. Freq. Control 61 251–65 [PubMed: 24474132]

Liney GP, Knowles AJ, Manton DJ, Turnbull LW, Blackband SJ and Horsman A 1996 Comparison of conventional single echo and multi-echo sequences with a fast spin-echo sequence for quantitative T2 mapping: application to the prostate J. Magn. Reson. Imaging 6603–7

Macoskey JJ, Choi SW, Hall TL, Vlaisavljevich E, Lundt JE, Lee FT, Johnsen E, Cain CA and Xu Z 2018a Using the cavitation collapse time to indicate the extent of histotripsy-induced tissue fractionation Phys. Med. Biol 63 055013 [PubMed: 29424711]

Macoskey JJ, Zhang X, Hall TL, Shi J, Beig SA, Johnsen E, Lee FT, Cain CA and Xu Z 2018b Bubble-induced color Doppler feedback correlates with histotripsy-induced destruction of structural components in liver tissue Ultrasound Med. Biol 44 602–12 [PubMed: 29329687]

Maxwell AD, Cain CA, Hall TL, Fowlkes JB and Xu Z 2013 Probability of cavitation for single ultrasound pulses applied to tissues and tissue-mimicking materials Ultrasound Med. Biol 39 449–65 [PubMed: 23380152]

Maxwell AD, Wang T-Y, Cain CA, Fowlkes JB, Sapozhnikov OA, Bailey MR and Xu Z 2011 Cavitation clouds created by shock scattering from bubbles during histotripsy J. Acoust. Soc. Am 130 1888–98 [PubMed: 21973343]

Maxwell AD, Wang T-Y, Yuan L, Duryea AP, Xu Z and Cain CA 2010 A tissue phantom for visualization and measurement of ultrasound- induced cavitation damage Ultrasound Med. Biol 36 2132–43 [PubMed: 21030142]

Metz CE 1978 Basic principles of ROC analysis Semin. Nucl. Med 8 283–98 [PubMed: 112681]

O ' Reilly MA, Jones RM and Hynynen K 2014 Three-dimensional transcranial ultrasound imaging of microbubble clouds using a sparse hemispherical array IEEE Trans. Biomed. Eng 61 1285–94 [PubMed: 24658252]

Otsu N 1979 A threshold selection method from gray-level histograms IEEE Trans. Syst. Man Cybern 9 62–6

Parsons JE, Cain CA, Abrams GD and Fowlkes JB 2006 Pulsed cavitational ultrasound therapy for controlled tissue homogenization Ultrasound Med. Biol 32 115–29 [PubMed: 16364803]

Partanen A et al. 2013 Magnetic resonance imaging (MRI)-guided transurethral ultrasound therapy of the prostate: a preclinical study with radiological and pathological correlation using customised MRI-based moulds BJU Int. 112 508–16 [PubMed: 23746198]

Partanen A, Farr N, Kreider W, Khokhlova T, Maxwell A, Wang Y-N, Bailey M and Khokhlova V 2014 Use of MRI to visualize mechanically fractionated lesions generated by boiling histotripsy in tissue Abstract Book of14th Int. Symp. for Therapeutic Ultrasound (2–5 April 2014, Las Vegas, Nevada, USA) (Online: https://istina.msu.ru/publications/article/6218863/)

Radhakrishnan K, Haworth KJ, Huang S-L, Klegerman ME, McPherson DD and Holland CK 2012 Stability of echogenic liposomes as a blood pool ultrasound contrast agent in a physiologic flow phantom Ultrasound Med. Biol 38 1970–81 [PubMed: 22929652]

Roberts WW 2014 Development and translation of histotripsy: current status and future directions Curr. Opin. Urol 24 104–10 [PubMed: 24231530]

Roberts WW, Hall TL, Ives K, Wolf JS, Fowlkes JB and Cain CA 2006 Pulsed cavitational ultrasound: a noninvasive technology for controlled tissue ablation (histotripsy) in the rabbit kidney J. Urol 175 734–8 [PubMed: 16407041]

Sahiner B, Pezeshk A, Hadjiiski LM, Wang X, Drukker K, Cha KH, Summers RM and Giger ML 2019 Deep learning in medical imaging and radiation therapy Med. Phys 46 e1–36 [PubMed: 30367497]

Salgaonkar VA, Datta S, Holland CK and Mast TD 2009 Passive cavitation imaging with ultrasound arrays J. Acoust. Soc. Am 126 3071–83 [PubMed: 20000921]

Schulman AA, Tay KJ, Robertson CN and Polascik TJ 2017 High-intensity focused ultrasound for focal therapy: reality or pitfall? Curr. Opin. Urol 27 138–48 [PubMed: 27997415]

Schuster TG, Wei JT, Hendlin K, Jahnke R and Roberts WW 2018 Histotripsy treatment of Benign prostatic enlargement using the Vortx Rx system: initial human safety and efficacy outcomes Urology 114 184–7 [PubMed: 29330000]

Shi A, Xu Z, Lundt J, Tamaddoni HA, Worlikar T and Hall TL 2018 Integrated histotripsy and bubble coalescence transducer for rapid tissue ablation IEEE Trans. Ultrason. Ferroelectr. Freq. Control 65 1822–31 [PubMed: 30040636]

Stejskal EO and Tanner JE 1965 Spin diffusion measurements: spin echoes in the presence of a time-dependent field gradient. J Chem. Phys 42 288–92

Stoica P, Wang Z and Li J 2003 Robust capon beamforming IEEE Signal Process. Lett 10 172–5

Vlaisavljevich E et al. 2016 Non-invasive ultrasound liver ablation using histotripsy: chronic study in an in vivo rodent model Ultrasound Med. Biol 42 1890–902 [PubMed: 27140521]

Vlaisavljevich E, Kim Y, Owens G, Roberts W, Cain C and Xu Z 2014 Effects of tissue mechanical properties on susceptibility to histotripsy- induced tissue damage Phys. Med. Biol 59 253–70 [PubMed: 24351722]

Wang TY, Xu Z, Winterroth F, Hall TL, Fowlkes JB, Rothman ED, Roberts WW and Cain CS 2009 Quantitative ultrasound backscatter for pulsed cavitational ultrasound therapy-histotripsy *IEEE Trans*. Ultrason. Ferroelectr. Freq. Control 56 995–1005

Wang T-Y, Xu Z, Hall TL, Fowlkes JB and Cain CA 2012 An efficient treatment strategy for histotripsy by removing cavitation memory Ultrasound Med. Biol 38 753–66 [PubMed: 22402025]

Xu Z, Hall TL, Fowlkes JB and Cain CA 2007 Optical and acoustic monitoring of bubble cloud dynamics at a tissue-fluid interface in ultrasound tissue erosion J. Acoust. Soc. Am 121 2421–30 [PubMed: 17471753]

Zhang X, Miller RM, Lin K-W, Levin AM, Owens GE, Gurm HS, Cain CA and Xu Z 2015 Real-time feedback of histotripsy thrombolysis using bubble-induced color Doppler Ultrasound Med. Biol 41 1386–401 [PubMed: 25623821]

Zhou Y-F 2011 High intensity focused ultrasound in clinical tumor ablation World J. Clin. Oncol 2 8–27 [PubMed: 21603311]

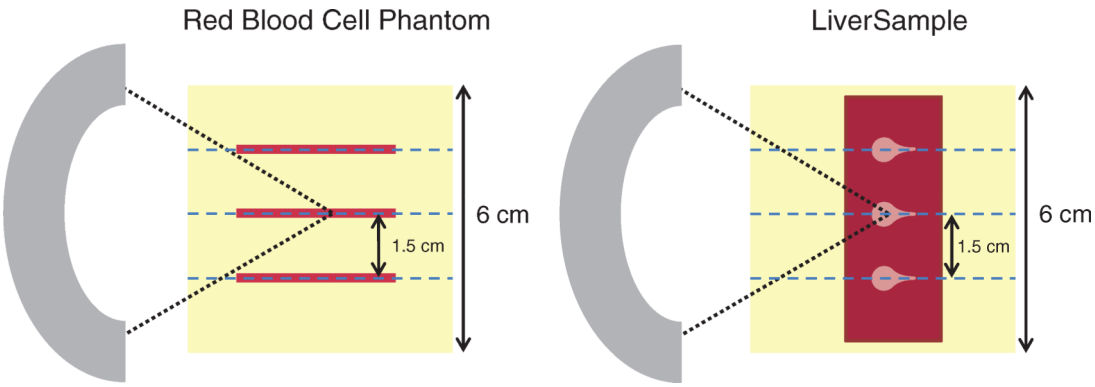

Figure 1.

Top-down view of experimental setup for phantoms containing red blood cell layers (left) and liver samples (right). Three locations were targeted with the therapy source (shown in gray on the left) in each phantom, separated by 1.5 cm. In red blood cell phantoms, agarose was poured in layers, with thin blood cell layers (red lines) applied via pipette on top of each solidified agarose layer. Additional fiducial markers (indicated by blue dotted lines) were used to orient the diagnostic ultrasound images, magnetic resonance (MR) images, and collected histologic samples parallel to the direction of ultrasound propagation.

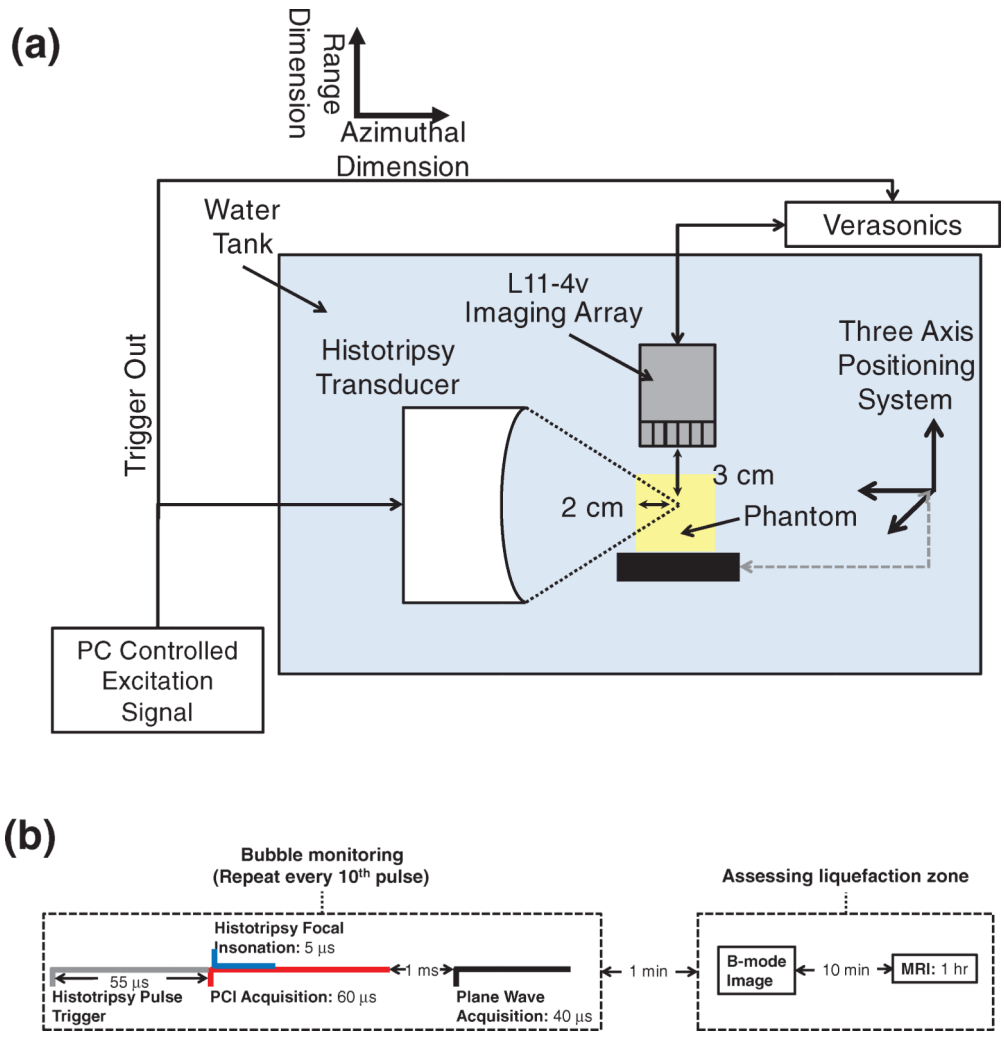

Figure 2.

(a) Side view of experimental setup for red blood cell (RBC) phantom insonation with a therapeutic ultrasound transducer. RBC layers of the phantoms were oriented parallel to the direction of ultrasound propagation from the histotripsy source. Fiducial markers embedded within the agarose were used to register diagnostic ultrasound and magnetic resonance (MR) images to digital photographs of phantoms post-insonation. The imaging plane of the L11–4v imaging array was registered to the RBC layers and visualized bubble activity along the acoustic axis of the histotripsy source. (b) Timeline of all image data acquisition. Passive and plane wave acquisitions were acquired every tenth histotripsy pulse due to data transfer rate limitations. Post hoc conventional B-mode images were acquired within 1 min of the histotripsy insonation. Samples were transferred to the MR scanner within 10 min, and MR images were acquired over the course of 1 h.

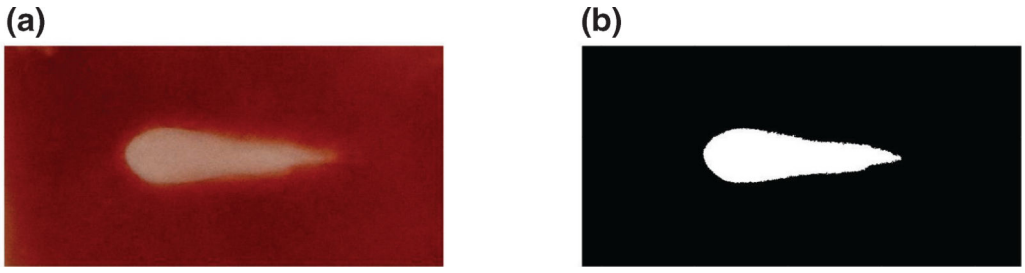

Figure 3.

Demonstration of Otsu thresholding to generate binary mask of liquefaction zone. Red-green-blue images (a) are converted to grayscale and a global threshold is determined based on the gray level histogram to generate a binary image (b).

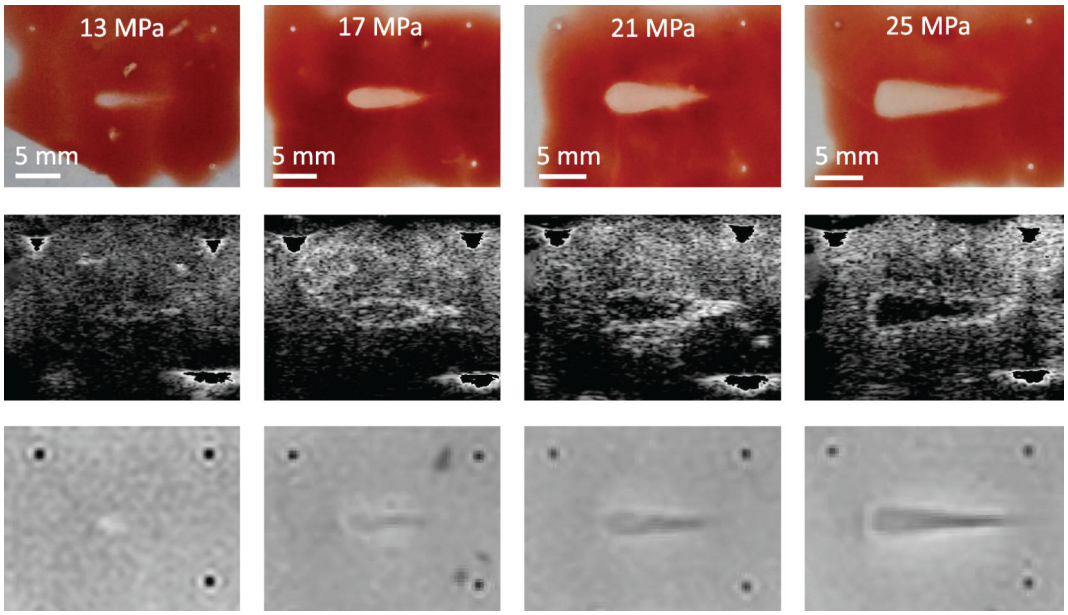

Figure 4.

Gross observations (top row) and post hoc visualizations of liquefaction zones with conventional B-mode images (middle row) and T_2-weighted images (bottom row). Insonations consisted of 13 (left) 17 (middle-left), 21 (middle-right), or 25 (right) MPa peak negative pressure pulses of 5 μs pulse duration and 1 MHz fundamental frequency in red blood cell phantoms. Therapeutic ultrasound pulses propagated from left to right in all images. In post-insonation conventional B-mode images, fiducial markers have been removed to allow better grayscale windowing for visualization of hypoechoic liquefaction zones.

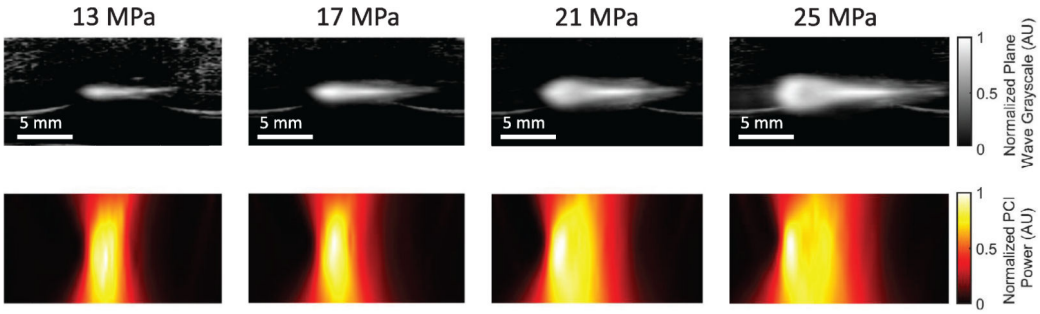

Figure 5.

Plane wave ultrasound images (top row) and passive cavitation images (bottom row) acquired during histotripsy insonation with 13 (left) 17 (middle-left), 21 (middle-right), and 25 (right) MPa peak negative pressure pulses of 5 μs pulse duration and 1 MHz fundamental frequency in red blood cell phantoms. Therapeutic ultrasound pulses propagated from left to right in all images.

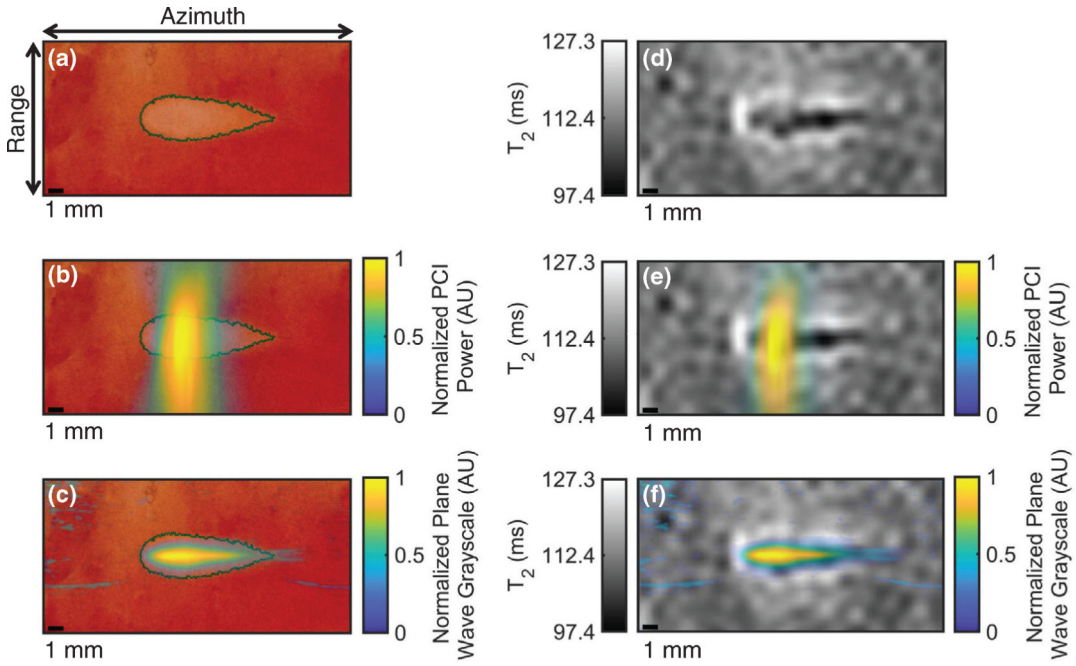

Figure 6.

Registration of imaging with gross observation of red blood cell phantom liquefaction. (a) Gross observation of liquefaction generated by histotripsy in a red blood cell phantom with the liquefaction zone outlined in green, (b) coregistration of passive cavitation imaging (PCI) acoustic power and red blood cell liquefaction, (c) coregistration of plane wave grayscale and red blood cell liquefaction, (d) parametric T_2 map of red blood cell liquefaction, (e) coregistration of PCI acoustic power and T_2 map, and (f) coregistration of plane wave grayscale and T_2 map. The liquefaction zone outline is shown in panels (a)-(c). The histotripsy pulse (1 MHz fundamental frequency, 5 μs pulse duration, 17 MPa peak negative pressure) propagated from left to right in the image. The azimuth/range dimensions of the diagnostic ultrasound imaging plane are indicated in the panel (a).

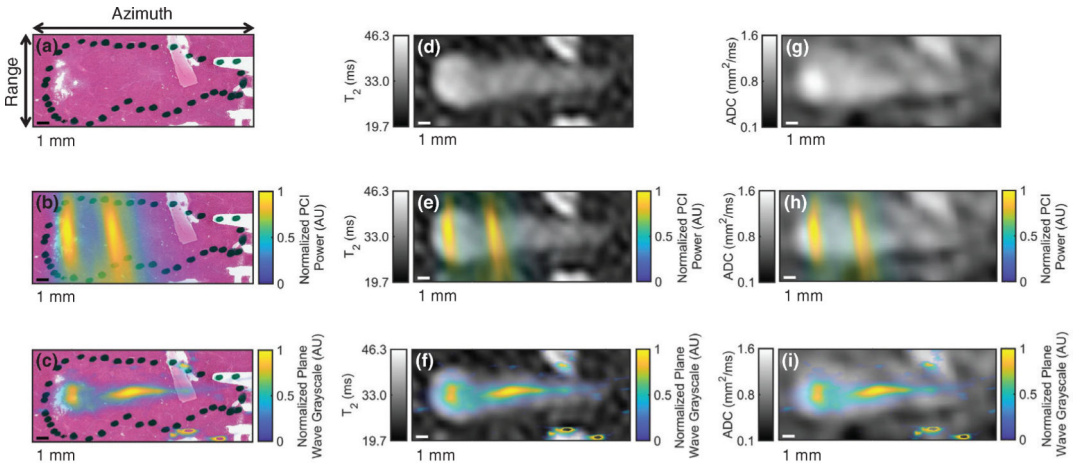

Figure 7.

Registration of imaging with histologic observation of liver sample liquefaction. (a) Hematoxylin and eosin (H&E) stain of liver sample exposed to histotripsy with the ablation zone indicated by the dotted black outline, (b) coregistration of passive cavitation imaging (PCI) acoustic power and H&E-stained liver sample, (c) coregistration of plane wave grayscale and H&E-stained liver sample, (d) parametric T_2 map of treated liver sample, (e) coregistration of PCI acoustic power and T_2 map, (f) coregistration of plane wave grayscale and T_2 map, (g) parametric apparent diffusion coefficient (ADC) map of treated liver sample, (h) coregistration of PCI acoustic power and ADC map, and (i) coregistration of plane wave grayscale and ADC map. The histotripsy pulse (1 MHz fundamental frequency, 5 μs pulse duration, 25 MPa peak negative pressure) propagated from left to right in the image. The azimuth/range dimensions of the diagnostic ultrasound imaging plane are indicated in the panel (a). Reflections from connective tissue in (c), (f), and (i) have been removed for better windowing and visualization of the histotripsy bubble cloud.

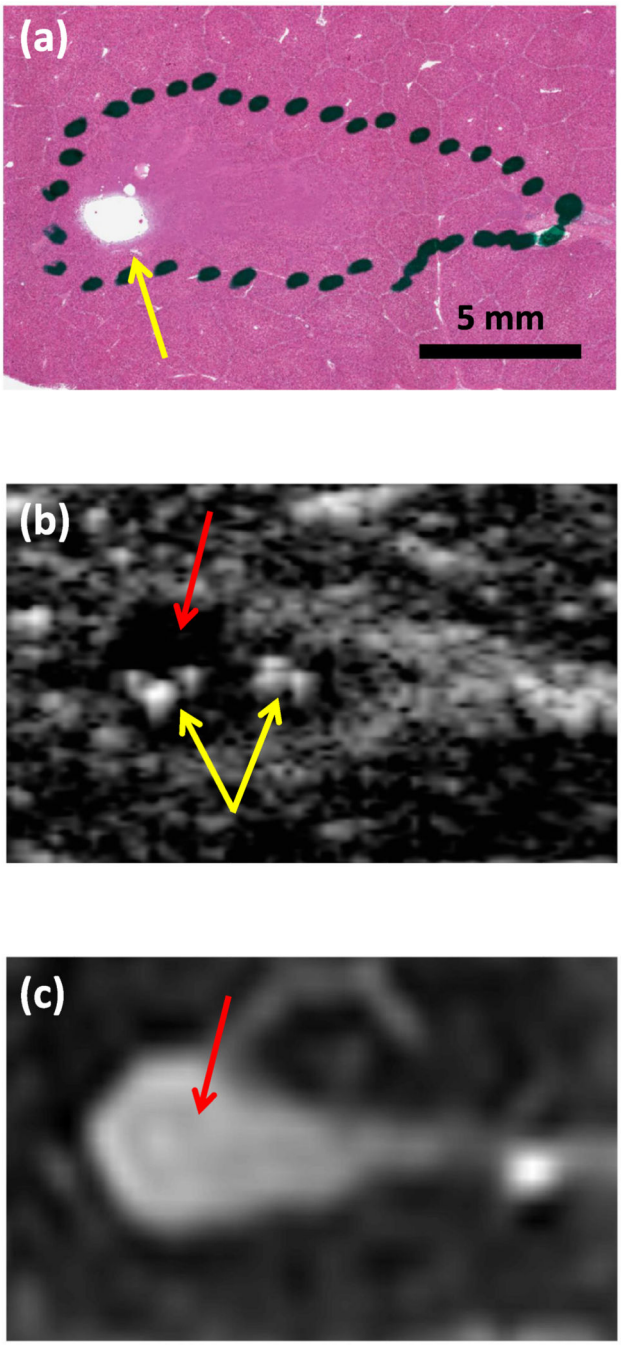

Figure 8.

Hematoxylin and eosin (H&E) stain, (b) post hoc conventional B-mode image, and (c) T_2-weighted image of liquefaction in the same liver sample. The liquefaction zone (dotted black dotted outline in (a), red arrows) can be distinguished as hypoechoic in (b) and hyperintense in (c). Regions of more thorough liquefaction exhibit minimal H&E staining, (yellow arrow in (a)). Small hyperechoic structures can be seen in the post hoc conventional B-mode image (yellow arrows in (b)), possibly indicating residual bubbles or accumulations of cellular

debris. The histotripsy pulse (1-MHz fundamental frequency, 5-μs pulse duration, 25-MPa peak negative pressure) propagated from left to right in each image.

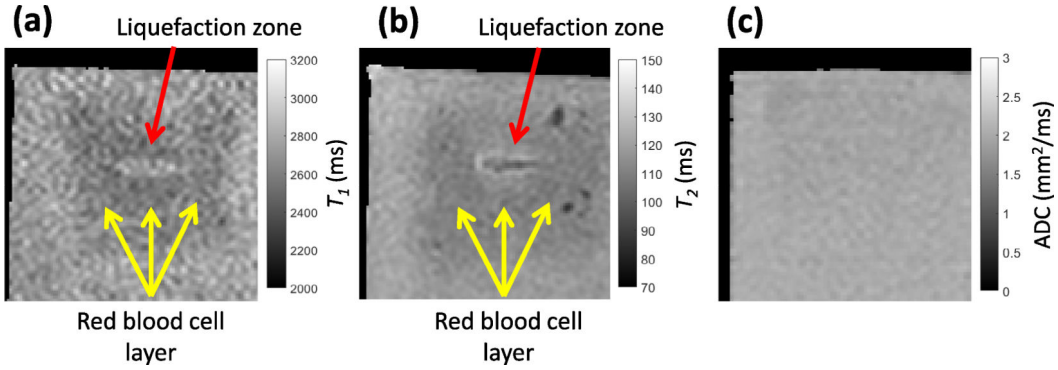

Figure 9.

Examples of parametric (a) T_1, (b) T_2, and (c) apparent diffusion coefficient (ADC) maps for red blood cell phantoms. The liquefaction zone is indicated by a red arrow in (a) and (b). The red blood cell layer (dark area) is indicated by yellow arrows in (a) and (b). The histotripsy pulse (1 MHz fundamental frequency, 5 μs pulse duration, 17 MPa peak negative pressure) propagated from left to right in each image.

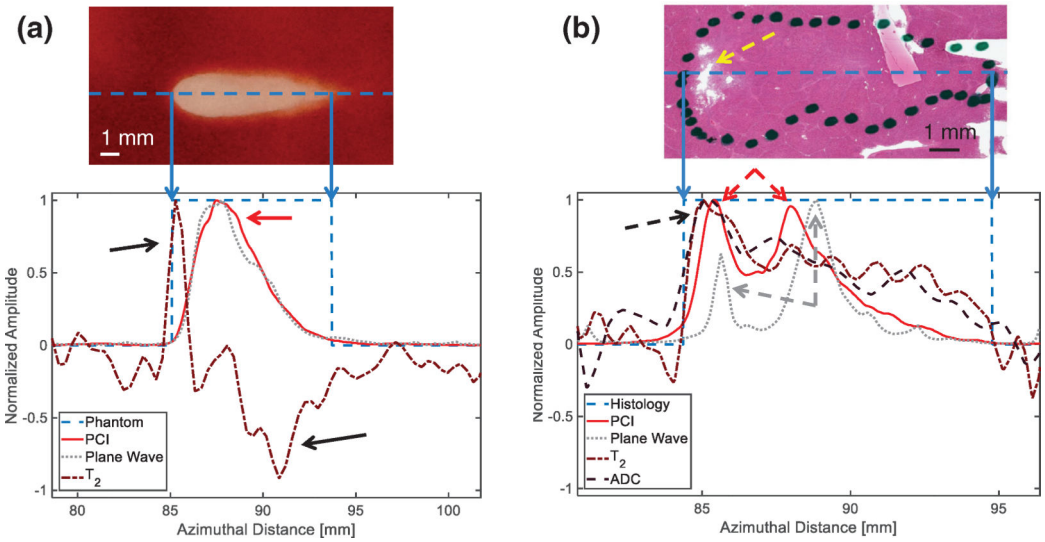

Figure 10.

Normalized amplitudes of passive cavitation imaging (PCI) acoustic power, plane wave grayscale, and change in T_2 from background along the central axis of the liquefaction zone (dashed blue line in top images) for (a) a red blood cell (RBC) phantom, and (b) a liver sample. The locations of liquefaction are binarized for the bottom plots, with values of 1 indicating liquefaction and 0 indicating intact media. The areas of greatest change in T_2 in the RBC phantom (black arrows) correspond to areas of relatively low PCI power and plane wave grayscale intensity (red arrow) within the liquefaction zone. In the liver sample, locations of T_2 and apparent diffusion coefficient maxima (black dashed arrows) correspond with more thorough liquefaction as indicated by Hematoxylin and eosin staining (yellow dashed arrow). Two maxima are present for PCI power (red dashed arrows) and plane wave grayscale (gray dashed arrows). The proximal (leftmost) plane wave grayscale peak is small compared with the distal (rightmost) peak, while the larger proximal PCI peak more accurately reflects the increased liquefaction and magnetic resonance parameter changes in this location. The histotripsy pulse (1 MHz fundamental frequency, 5 μs pulse duration, 17 MPa peak negative pressure for RBC phantom, 25 MPa peak negative pressure for liver sample) propagated from left to right in each image.

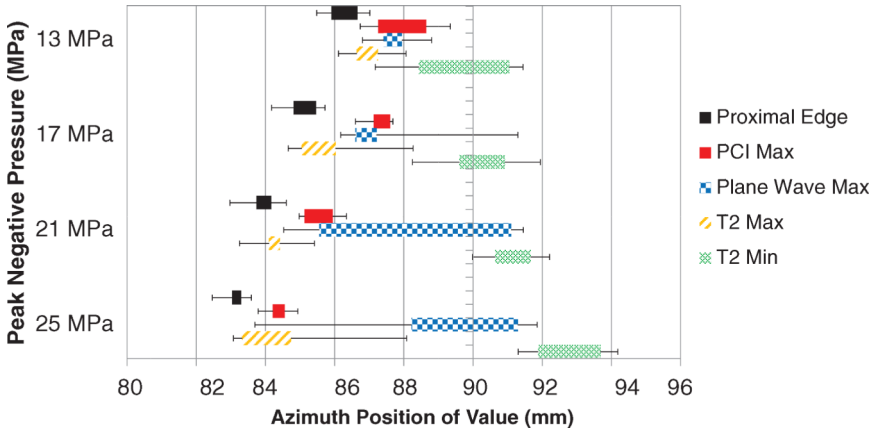

Figure 11.

Azimuthal position of proximal edge of liquefaction zone (solid black bars), maximum passive cavitation imaging (PCI) acoustic power (solid red bars), plane wave grayscale (checkered blue bars), and maximum (striped orange bars) and minimum (cross-hatched green bars) T_2 for all pressures applied to red blood cell phantoms. Colored bars cover 25% to 75% quantiles, and error bars extend to maximum and minimum azimuthal positions recorded for each parameter. 90 mm corresponds to the geometric focus of the histotripsy source. Locations of maximum PCI acoustic power and T_2 shift proximally with increasing pressure, while plane wave maxima and T_2 minima shift distally.

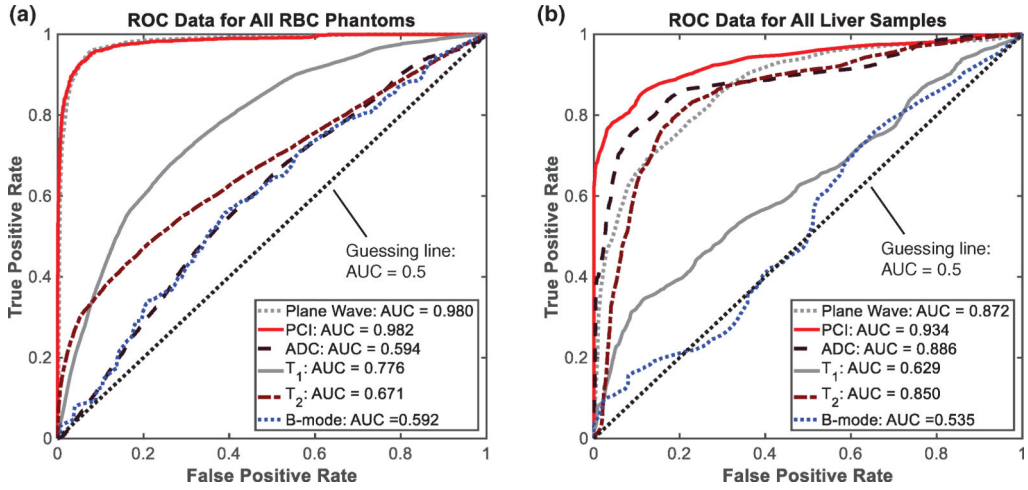

Figure 12.

Receiver Operating Characteristic (ROC) curves obtained from (a) red blood cell phantoms and (b) liver samples. Quantitative plane wave grayscale (gray dotted line), passive cavitation imaging acoustic power (red solid line), apparent diffusion coefficient (black dashed line), T_1, (gray solid line), T_2, (brown dash-dot line), and post hoc conventional B-mode grayscale (blue dotted line) were used to predict presence of liquefaction/necrosis along azimuth dimension of histotripsy lesions across all peak negative pressures of the histotripsy pulse (only 1 pressure level was employed in the liver studies). The black dotted line indicates the resulting ROC curve from random guessing (area under the curve = 0.5).

Table 1.

MR scan parameters used for 3 T imaging and parametric mapping of T_1, T_2, and ADC.

Sequence	TR/TE (ms)	In-plane resolution (acquisition) (mm^2)	Array size (recon matrix)	Slice thickness (mm)	NSA	Echo factor	TI (ms)	*b*-values ($s\ mm^{-2}$)
T_1W SE	600/10	1.0 × 1.0	192 × 192	2	2	N/A	N/A	N/A
T_2W TSE	4000/100	0.7 × 0.7	224 × 224	2	4	16	N/A	N/A
T_1 mapping (IR)	7000/7	0.7 × 0.7	224 × 224	2.5	1	6	50, 100, 250, 500, 750, 1000, 2500, 5000	N/A
T_2 mapping (multi-echo SE)	4000/20, 40, 60, 80, 100	0.7 × 0.7	224 × 224	2.5	2	5	N/A	N/A
ADC mapping for RBC phantoms (DWI EPI)	5000/160	1.0 × 1.0	384 × 384	3	12	115 (EPI)	N/A	0, 250, 500, 750, 1000
ADC mapping for liver samples (DWI EPI)	5000/69	1.2 × 1.2	176 × 176	4	24	27 (EPI)	N/A	0, 250, 500, 750

TR/TE = repetition time/echo time; NSA = number of signal averages; TI = inversion time; T_1W/T_2W = T_1-/T_2-weighted; SE/TSE = spin echo/turbo spin echo; IR = inversion recovery; ADC = apparent diffusion coefficient; DWI = diffusion-weighted imaging, and EPI = echo planar imaging.

Phys Med Biol. Author manuscript; available in PMC 2020 May 02.

Table 2.

Diagnostic ultrasound and MR parameter values measured within liquefaction zones for RBC phantoms insonated at peak negative pressures of 13, 17, 21 and 25 MPa, and liver samples insonated at 25 MPa.

	RBC phantoms				Liver samples
Image parameters	**13 MPa**	**17 MPa**	**21 MPa**	**25 MPa**	**25 MPa**
Bubble activity monitoring					
PCI acoustic power ($\times 10^5$ V^2)	0.17 ± 0.06[a]	1.03 ± 0.26[a]	1.48 ± 0.21[a]	1.82 ± 0.15[a]	1.33 ± 0.41[a]
Plane wave grayscale ($\times 10^8$)	1.31 ± 0.54[a]	6.09 ± 2.26[a]	7.98 ± 2.27[a]	7.63 ± 3.08[a]	6.41 ± 2.26[a]
Post hoc evaluation					
Post hoc conventional B-mode grayscale ($\times 10^8$)	0.43 ± 0.18	0.56 ± 0.47	0.42 ± 0.17	1.82 ± 3.77	34.9 ± 57.8
T_1 (ms)	2645 ± 83[a]	2673 ± 55[a]	2657 ± 56[a]	2647 ± 44[a]	296 ± 150
T_2 (ms)	123 ± 4[a]	119 ± 4[a]	117 ± 6[a]	117 ± 7[a]	35.0 ± 2.7[a]
ADC (mm^2 ms^{-1})	1.97 ± 0.04	1.97 ± 0.04[a]	1.98 ± 0.05	1.98 ± 0.04[a]	0.89 ± 0.10[a]

[a]Liquefaction zone significantly different from background (untreated) phantom/tissue.

Note: all errors are given as standard deviations.

Table 3.

Area under the curve (AUC) values calculated for all RBC phantom data, and sensitivities, specificities, accuracies, positive predictive values (PPV), and negative predictive values (NPV) at optimal threshold points for all ROC curves.

Image parameter	Optimal threshold value (95% confidence interval)	AUC	Sensitivity	Specificity	Accuracy	PPV	NPV
PCI acoustic power × 10^4 V^2	1.17 [1.17, 1.19]	0.982	**0.896**	0.969	0.947	0.926	0.955
Plane wave grayscale × 10^8 grayscale value	1.03 [0.80, 1.09]	**0.980**	**0.884**	**0.967**	**0.942**	**0.921**	**0.950**
T_1 (change in ms)	65 [56, 66]	**0.776**	**0.495**	0.865	0.753	0.616	**0.797**
T_2 (absolute change in ms)	7.24 [7.16, 7.62]	**0.671**	**0.299**	0.949[a]	**0.751**	0.718[a]	**0.756**
ADC[b] (change in mm^2 ms^{-1})	0.195 [0.192, 0.195]	0.594	0.000	**1.000**[a]	0.696	N/A	0.696
Post hoc conventional B-mode × 10^9 (absolute change in grayscale value)	5.09 [5.09, 5.09]	0.592	0.034[a]	0.992	0.701	0.659	0.702

Note: image parameters are listed in order of greatest to lowest AUC values.

Bold text indicates statistic is significantly greater than that of subsequent (next lowest) parameter in left column.

[a]Indicates statistic significantly greater than that of preceding (next highest) parameter in left column.

[b]Chosen threshold point resulted in 100% negative classifications.

Table 4.

Area under the curve (AUC) values calculated for all liver sample data, and sensitivities, specificities, accuracies, positive predictive values (PPV), and negative predictive values (NPV) at optimal threshold points for all ROC curves.

Image parameter	Optimal threshold value (95% confidence interval)	AUC	Sensitivity	Specificity	Accuracy	PPV	NPV
PCI power × 10^3 V^2	7.055 [7.046, 7.435]	**0.934**	**0.862**	**0.882**	**0.871**	**0.885**	0.858
ADC (change in mm^2 ms^{-1})	0.13 [0.11, 0.22]	**0.886**	0.839	**0.828**	**0.833**	**0.837**	0.830
Plane wave grayscale × 10^8 grayscale value	0.65 [0.60, 1.27]	**0.872**	**0.853**	0.708	0.783	0.755	0.821
T_2 (change in ms)	3.5 [3.1, 4.1]	**0.850**	**0.810**	0.799[a]	**0.804**	**0.809**[a]	**0.800**
T_1 (change in ms)	41 [40, 45]	**0.629**	0.342	**0.886**[a]	**0.621**	**0.741**	0.586
Post hoc conventional B-mode × 10^8 (absolute change in grayscale value)	7.08 [6.61, 7.57]	0.535	0.759[a]	0.345	0.558	0.550	0.577

Note: image parameters are listed in order of greatest to lowest AUC values.

Bold text indicates statistic is significantly greater than that of subsequent (next lowest) parameter in left column.

[a]Indicates statistic significantly greater than that of preceding (next highest) parameter in left column.

Table 5.

DSC values ± standard deviations as a function of peak negative pressure and tissue/phantom type.

	Red blood cell phantoms					Liver samples
	13 MPa	**17 MPa**	**25 MPa**	**25 MPa**	**All pressures**	**25 MPa**
Conventional B-mode images	0.68 ± 0.11	0.81 ± 0.11	0.83 ± 0.05	0.85 ± 0.08	0.79 ± 0.11	0.49 ± 0.15
T_2W images	0.77 ± 0.10[a]	0.87 ± 0.06	0.91 ± 0.02[a]	0.91 ± 0.02[a]	0.87 ± 0.08[a]	0.77 ± 0.06[a]

[a]Indicates significantly greater DSC value from T_2W images over post hoc conventional B-mode images.

Note: errors represent standard deviations over samples.